Proton precipitation in Mercury's northern magnetospheric cusp

Jim M. Raines (1), Ryan M. Dewey (1), Natalie M. Staudacher (1), Patrick J. Tracy (1), Christopher M. Bert (1), Menelaos Sarantos (2), Daniel J. Gershman (2), Jamie M. Jasinski (3), Charles F. Bowers (1), Erik Fisher (1), and James A. Slavin (1)

(1) Climate and Space Sciences and Engineering, University of Michigan, Ann Arbor, Michigan, USA.
(2) Geospace Physics Laboratory, NASA Goddard Space Flight Center, Greenbelt, Maryland, USA.
(3) NASA Jet Propulsion Laboratory, California Institute of Technology, Pasadena, CA, USA.

1 Abstract

Ion precipitation onto Mercury's surface through its magnetospheric cusps acts as a source of planetary atoms to both Mercury's exosphere and magnetosphere. Through the process of ion sputtering, solar wind ions (~95% protons) impact the surface regolith and liberate material, mostly as neutral atoms. We have identified 2760 northern magnetospheric cusp crossings throughout the MErcury Surface, Space ENvironment, GEochemistry and Ranging (MESSENGER) mission, based on enhancements in proton flux observed by the Fast Imaging Plasma Spectrometer (FIPS). We find cusp crossings spanning 50-85° in magnetic latitude with a geometric center typically at 60-70°. The cusp center is stable about its average but its latitudinal extent varies orbit-to-orbit. The mean latitude weakly depends on the magnitude of the interplanetary magnetic field (IMF), dropping by about 1.3° magnetic latitude for each increase of 10 nT in IMF strength. We have used these identified cusp boundaries to estimate the flux of protons which will precipitate onto Mercury's surface. We find an average proton precipitation flux of 1.0×10^7 cm^{-2} s^{-1}, ranging $3.3 \times 10^4 - 6.2 \times 10^8$ cm^{-2} s^{-1}, and that this flux can vary substantially between subsequent 10-s measurements. We also tabulated the peak precipitation fluxes for each cusp crossing. They range $9.8 \times 10^4 - 1.4 \times 10^9$ cm^{-2} s^{-1}, with a mean of 3.7×10^7 cm^{-2} s^{-1}. We find strong dependencies on the local time of the cusp crossing as well as on Mercury's orbit around the Sun, which warrant further investigation.

2   Introduction

Impact of solar wind ions and electrons around Mercury's northern magnetospheric cusps is believed to act as a significant and highly variable source to the planet's exosphere (thin atmosphere) and magnetosphere [e.g. Killen et al., 2007; Milillo et al., 2005]. The ~1 keV ion component imparts enough energy on the surface to release neutral atoms (>90%) and ions (<10%) into the exosphere [Lammer et al., 2003] in a process known as ion sputtering (IS). Solar wind electrons of 1-10 eV liberate particles in a related process known as electron-stimulated desorption (ESD) [*McLain et al.*, 2011]. Mercury's exosphere is too tenuous to serve as the magnetosphere's inner boundary so the two are collocated above Mercury's surface. IS and ESD therefore serve as a direct source to the exosphere, as well as to the magnetosphere. Despite significant work in this area, both through space-based observations [e.g. Vervack et al., 2010; 2016; Cassidy et al., 2015; Merkel et al., 2017], ground-based observations [e.g. Potter et al., 2006; Killen et al. 2007; 2010; 2016; Mangano et al., 2015; Orsini et al, 2018] and exospheric modeling ['Lebland and Johnson, 2003; Sarantos et al., 2007; 2011; Burger et al., 2012; 2014], no clear consensus has emerged concerning the contribution of ion sputtering to either the exosphere or magnetosphere relative to other source processes. One key piece of this puzzle is the fluxes of ions impacting the surface (i.e., precipitation).

The mechanism for entry of solar wind plasma into the cusp is reconnection of the interplanetary magnetic field (IMF) with the planetary field on the surface of the dayside magnetopause. These recently reconnected field lines are dragged over the poles of the planet and into the magnetotail as the solar wind flows by the magnetosphere. Solar wind ions and electrons, bound to these recently reconnected field lines and energized by the reconnection process, travel to the magnetospheric cusps where they precipitate onto the surface or reflect in the magnetic mirror. This reconnection has been studied extensively at Earth [e.g Sonnerup et al., 1981] and at Mercury [e.g. Slavin et al., 2009; DiBraccio et al., 2013; Gershman et al., 2013; Imber et al., 2014] using data from the MErcury Surface, Space Environment, GEochemistry and Ranging (MESSENGER) mission [Solomon et al., 2007]. Fluxes of energetic electrons during Solar Energetic Particle (SEP) events were enhanced over the polar cap region, including the cusp, providing further support that cusp field lines are open and connected to the IMF [Gershman et al., 2015; 2016].

The flux of these precipitating ions has been predicted by many numerical simulations. Kallio and Janhunen [2003] used a hybrid simulation to predict precipitation of solar wind protons under a wide range of solar wind and IMF conditions. They found under normal solar wind conditions that the solar wind plasma precipitates in well-defined bands at mid-latitudes on the dayside centered around the magnetospheric cusps. Estimating from their Figure 3, these bands were reasonably uniform spatially, with fluxes of up to about 10^8 cm^{-2} s^{-1}, and were about the same for the two orientations tested, pure northward and pure southward IMF B$_z$. Under very high solar wind flux conditions, with a density and speed of 76 cm^{-3} and 860 km/s, respectively, their simulations showed that solar wind protons would precipitate over a broad region on the dayside including the subsolar point and connecting the two high latitude bands. Precipitating flux in those cases reached up to about 10^9 cm^{-2} s^{-1}. A subsequent work based on a newer version of the same hybrid model with new sets of solar wind cases and post-MESSENGER planetary magnetic field values revisited the rates of precipitation and resultant exospheric generation [Pfleger et al., 2015]. That work reported similar precipitation patterns, though the most intense precipitation regions show up to 10x higher precipitation flux, 10^{10} cm^{-2}

s^{-1} (estimated from their Figure 1). As in the original work, modeled precipitating flux in the cusp region showed some dependence on IMF orientation in the three cases of nominal conditions (ignoring their extreme solar wind case, 4). Both the flux and the area of precipitation in the cusp region were larger for normal and dense solar wind flows than for northward IMF. The total change in precipitation rate for these three cases was not reported, but appears to be less than a factor of 10. Their modeled exospheric column densities followed the same trends, consistent with their finding that sputtering is an important source for Mercury's exosphere. Fatemi et al. [2020] reported precipitating proton fluxes in the same range, $0.5\text{-}1.0 \times 10^9$ cm^{-2} s^{-1}, derived from their hybrid model [Fatemi et al., 2018]

Other modelers have taken a different approach to making the same predictions. Benna et al. [2010] used a fluid magnetohydrodynamic (MHD) model in which the planetary field had been adjusted to closely match the magnetic field measurements from MESSENGER in its first flyby of Mercury in 2008. Under the particular solar wind conditions of that flyby, the MHD model showed peaks in precipitating flux of $\sim 2 \times 10^8$ cm^{-2} s^{-1}, focused, again, at high latitudes in the magnetospheric cusps. Massetti et al. [2003] used an average magnetic field model from the Earth, adjusted to Mercury, then applied an analytical model to compute the precipitating proton flux. Their results were close to the other methods, reporting fluxes of about 4×10^8 cm^{-2} s^{-1} for several different IMF Bz values.

Several estimates of average proton precipitation flux from MESSENGER observations have also been made. Winslow et al. [2014] developed a technique called "proton reflectometry" using proton loss cone measurements averaged over about 800 orbits to estimate the magnetic field at Mercury's surface. Using average proton density and temperature in the cusp, they reported an estimated proton precipitation flux in the northern cusp of 3.7×10^8 cm^{-2} s^{-1}. Poh et al. [2016] analyzed very deep depressions (up to 90%) in the magnetic field measured by MESSENGER over very short times (~3 sec). Termed "cusp filaments" since they are observed in and around the cusp [Slavin et al, 2014], these cylindrical flux tubes appear to carry magnetosheath plasma down to the surface, with an estimate precipitation rate of 2.7×10^{25} s^{-1}. Using their estimated cusp filament diameter of 105 km, this works out to a precipitation flux of 7.8×10^{10} cm^{-2} s^{-1}. Both of these estimates are in good agreement with model predictions, adding the consideration that cusp filaments likely represent extreme precipitation fluxes that are expected to be far from the mean.

Laboratory experiments on soil simulants have revealed much concerning the effects of solar wind plasma impact on Mercury's surface through IS and ESD, but there are still significant unknowns. For example, the sputtering yield, the ratio of incident ions to sputtered particles, ranges from 0.04 to 0.08 for Na sputtered by H+ in the solar wind energy range $(0.5 - 2$ keV), assuming a binding energy of Na to surface O of 2-2.65 eV [Lammer et al., 2003]. In ESD, sodium is desorbed by electrons with energies as low as 4 eV [Yashinskiy and Madey, 2000], which are consistently present in the solar wind. The elemental composition of the liberated species should reflect the surface composition, but a particular parcel can become depleted in certain elements by repeated bombardments. As such, the history of plasma impact is also important. These processes, known collectively as "space weathering", can also change the spectral properties of the surface materials and are thus broadly relevant in the study of airless bodies by remote sensing [Domingue et al, 2007; 2014]. However, lab tests are run on very well-defined materials, stoichiometric, crystalline oxides, whereas Mercury's surface regolith is much more poorly defined, likely non-stoichiometric and amorphous. Na binding

energy listed above is a perfect example of unknown details: Other experiments, using a different soil simulant, yielded a value of the Na binding energy lower by almost 10x, 0.27 eV [Wiens et al., 1997], a change which greatly effects the sputtering yields. Furthermore, Mercury's surface is very likely charged and that probably plays a role, as does the altered binding of alkali atoms to the surface caused by irradiation. Quantitative rates of removal are simply not yet available [Madey et al., 1998].

In this work, we contribute a key piece previously missing from this puzzle: the first precipitation fluxes and rates for individual cusp crossings in Mercury's northern magnetospheric cusp. We have computed these from observations by the MESSENGER mission, in 2760 crossings of Mercury's northern magnetospheric cusp. This set represents all the identifiable cusps, according to our criteria below, in the 4106 orbits where MESSENGER plasma data is available. This paper is organized as follows: First we discuss the data and methods used to estimate precipitating flux. Next, we show the data used in this study both as time series and as directional histogram. We then show our estimates of precipitating flux and precipitation rate for 2760 cusp crossings and examine the dependencies of those fluxes on expected spatial and temporal quantities. Finally, we compare our estimates to previous predictions and discuss the results.

3 Observations

We used data from the Fast Imaging Plasma Spectrometer (FIPS) [Andrews et al., 2007]. During this phase of the mission, FIPS measured ions with energy per charge (E/q) from 50 eV/e to 13 keV/e, sweeping through those energies to make a full energy spectrum about every 10s. FIPS is a unique instrument with a large, 1.4 π sr *simultaneous* field of view (FOV), though it was reduced due to placement on the spacecraft to 1.15 π sr. Magnetic field measurements in this study were made with the MESSENGER Magnetometer (MAG) [Anderson et al., 2007]. Data used for this study was acquired throughout the entire
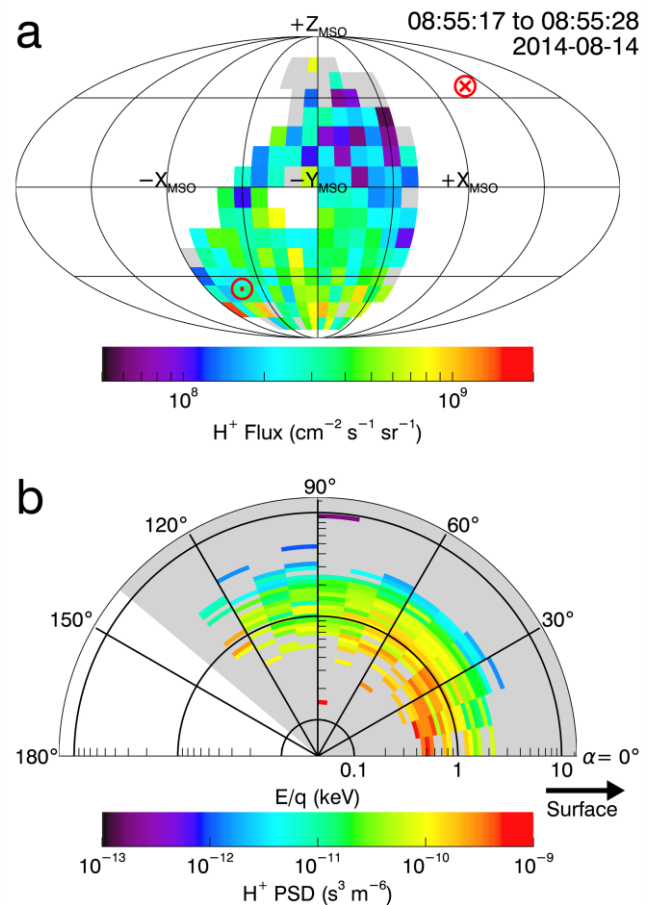

Figure 1. (a) Angular flux map (AFM) and (b) energy-resolved pitch-angle (ERPA) distribution of protons observed by FIPS during a cusp crossing on 14-Aug-2014. Both maps show protons flowing into the cusp. The ERPA also shows evidence of precipitation through a 50-60° loss cone. The red circled dot and circled x symbols represent the parallel and antiparallel directions to the magnetic field, respectively.

MESSENGER orbital mission, during the period of 06 Apr 2011 through 30 Apr 2015. FIPS measured the velocity vector for each ion event, consisting of the magnitude plus two incident angles: zenith and azimuth in the instrument frame. These vectors were transformed into Mercury Solar Orbital (MSO) coordinates, a reference frame centered on Mercury with an X_{MSO} component that points toward the Sun and a Z_{MSO} component that points perpendicular to the ecliptic plane (and Mercury's equatorial plane). These transformed ion events were then histogrammed in all three of these dimensions and integrated over the magnitude dimension to produce a 2D angular flux map for each 10s E/q scan (Figure 1a). The resulting map gives the directional flux of the measured ions in MSO coordinates [Raines et al., 2014; Gershman et al., 2014]. The map in this example shows that protons are flowing mainly along the $-Z_{MSO}$ direction (down in the figure). Since MESSENGER was over the cusp at the time, this equates to flowing toward the surface, into the cusp. The direction of the magnetic field and its opposite are shown by the circled dot and circled x symbols, respectively. The transformed velocity vectors were also combined with magnetic field vectors measured over the same period to compute the pitch angle, the angle between the two vectors. Pitch angles were collected into 10° angle bins, separated by the intrinsic E/q steps of the instrument. This created an energy-resolved pitch angle distribution (ERPA) [Raines et al., 2014; Gershman et al., 2014] for each scan. An example ERPA is shown in Figure 1b. Zero pitch angle is along the right edge and increases counter-clockwise. Energy increases with increasing radius, labeled at 0.1, 1.0 and 10 keV. Bins are colored by phase space density in $s^3 m^{-6}$. On these figures, portions of the distribution corresponding to pitch angles outside of FIPS FOV at that time are colored white (unobserved). This map also shows protons flowing into the cusp; the flux is most intense within 30° of the magnetic field direction, i.e., towards the planet's northern hemisphere surface. The absence of flux at large pitch angles, beginning at 120-130°, is evidence of a 50-60° loss cone where protons are precipitating onto the surface and are thus unable to reflect off of the magnetic field to fill this area of the map with upwelling (reflected) protons.

The orientation of the FIPS FOV can have an effect on the measured ion fluxes, particularly relative to the direction of the magnetic field. For this study, we differentiate between scans when the magnetic field direction (or its negative) was within the FIPS FOV and when it was not. In the former case, this requirement ensures that the entire parallel component of the ion distribution is included in the precipitating flux estimation, a least during the majority of the cusp crossing. We use these cases for our quantitative evaluation of precipitation flux.

In all cases, we assume that the distribution is symmetric about the field, i.e. gyrotropic, which is very likely true to at least to first order on the 10 s time scales in question. At 200 nT, the proton gyroperiod is 0.3 s. The usual cross-magnetosphere electric field is ~2 mV/m [Jasinski et al., 2017; Dewey et al., 2018] so this translates to an ExB drift of 10 km/s. At this convection speed, the magnetic field lines move only ~3 km in a proton gyroperiod, which is much smaller than a proton gyroradius (23 km for 1 keV, 90-deg pitch angle proton). The change in the magnetic field over the 3 km is <2%. The subsonic, slow convection speed and the small change in the magnetic field intensity indicate protons should be gyrotropic and adiabatic.

4   Estimating precipitating flux

When approaching the surface of Mercury in the cusp, ions flowing down magnetic field lines will impact the surface (i.e., precipitate) if they have sufficient velocity parallel to the magnetic field to overcome the magnetic mirroring force produced by the magnetic field at the

surface. Under a small set of assumptions, the precipitation flux for protons at the surface can be estimated from measurements of particle energy, pitch angle and magnetic field in orbit. Our first assumption is that the particles behave adiabatically, meaning that their magnetic moment, the ratio of energy perpendicular to the magnetic field to the strength of the field itself, is constant. This assumption is accurate when the magnetic field changes over spatial or temporal scales much larger than the proton gyroradius and gyroperiod, respectively, as is expected in the cusp (see above). Our second assumption is that the magnetic field is nearly radial and can be approximated by that of a dipole, e.g. falling off as $1/R^3$, where R is the radial distance from the center of the dipole. In the cusp, with altitudes <1000 km, these assumptions are quite reasonable. The field is nearly dipolar and oriented radially. Proton gyro radii are relatively small, ~10-50 km, compared to the width of the cusp perpendicular to the magnetic field (>400 km), so that non-adiabatic effects can be neglected to first order.

The precipitating flux for a single FIPS energy scan was estimated using the following procedure. First, the magnetic field at the surface (B_1) is computed as a dipolar field fall-off ($1/R^3$) from the value measured at the spacecraft (B_0). In Equation 1, r_0 is the radial distance from the magnetic dipole center to the spacecraft and r_1 is the distance from the dipole center to the planetary surface along r_0. Mercury's magnetic dipole is offset by 484 km northward of the planet's center [*Anderson et al.*, 2011]. The surface field is on the average 1.5 times higher than that measured at the spacecraft, with 96% falling under 2.1 times higher.

$$B_1 = B_0 \frac{r_1^3}{r_0^3} \tag{1}$$

Second, we used the pitch angle measured by FIPS (α_0) to compute the components of the original velocity vector (v_0), parallel ($v_{\parallel 0}$) and perpendicular ($v_{\perp 0}$) to the magnetic field vector (Equations 3 & 4). We computed the magnitude of the original velocity vector (v_0), using the measured E/q and charge per mass (q/m in e/amu) [Gloeckler et al, 1998].

$$v_0 = 438 \sqrt{\left(\frac{E}{q}\right)\left(\frac{q}{m}\right)} \tag{2}$$

$$v_{\parallel 0} = v_0 \cos \alpha_0 \tag{3}$$

$$v_{\perp 0} = v_0 \sin \alpha_0 \tag{4}$$

Under the assumption of adiabatic behavior of the ions, Liouville's theorem can be used to map the observed ERPA distribution (Figure 1b) from the spacecraft to the surface [Gershman et al., 2017]. We over-sampled the ERPA from the native 10° bins to 2° bins to reduce errors due to rounding and truncation at 90°. This allows us to recompute the velocity components at the surface

$$v_{\parallel 1} = \sqrt{v_{\perp 0}^2 \left(1 - \frac{B_1}{B_0}\right) + v_{\parallel 0}^2} \tag{5}$$

$$v_{\perp 1} = \sqrt{v_{\perp 0}^2 \left(\frac{B_1}{B_0}\right)} \tag{6}$$

And use those new velocity components to compute the new pitch angle (α_1),

$$v_1 = \sqrt{v_{\parallel 1}^2 + v_{\perp 1}^2} \tag{7}$$

$$\alpha_1 = \cos^{-1}\left(\frac{v_{\parallel 1}}{v_1}\right) \tag{8}$$

Finally, the resulting distribution was integrated over pitch angles 0-90° and over the full range of FIPS energies to compute the precipitating flux. This amounts to integrating over the right quarter circle in Fig. 1b. Specifically, the precipitating flux ($J_1/\Delta t$) is determined by summing over all 60 energy and 45 pitch angle bins, $0 < \alpha_j < \pi/2$, using formula below. Units are all SI. The ERPA (h_E) is in units of phase space density in $s^3\ m^{-6}$. Additional details regarding such integrations can be found in Tracy [2016].

$$\frac{J_1}{\Delta t} = 4\pi \left(\frac{q}{m}\right)^2 \sum_{i=0}^{59} \left(\frac{E}{q}\right)_i \left[\sum_{j=0}^{44} \cos \alpha_j \sin \alpha_j\ h_E\left(\left(\frac{E}{q}\right)_i, \alpha_j\right)\Delta\alpha\right]\left(\frac{\Delta E}{q}\right)_i \tag{9}$$

$$\left(\frac{\Delta E}{q}\right)_i = \begin{cases} \left(\frac{E}{q}\right)_0 & i = 0 \\ \left(\frac{E}{q}\right)_i - \left(\frac{E}{q}\right)_{i-1} & i > 0 \end{cases} \tag{10}$$

5 Cusp Identification and Examples

We identified crossings of Mercury's northern magnetospheric cusp as areas of enhanced plasma flux on the dayside that lie between the dayside closed-field magnetosphere and the northern magnetic lobe of the magnetotail. This was done in two stages: First, we identified these enhancements by eye using the same method for identifying cusp crossings as Raines et al. [2014]. In this selection, we look for a period of enhanced plasma flux on the dayside, typically separated from other enhanced periods and at having only the lower energy component when compared to the magnetosheath observations. Second, we applied a software algorithm to regularize and trim these boundaries based on a simple set of principles. The algorithm is described in Appendix A.

These are different criteria than are typically used at Earth, where the cusp is often identified largely on the basis of magnetic depressions [Lavraud et al., 2004; 2005]. Several other studies have identified cusp crossings at Mercury from the magnetic field alone (Winslow et al., 2012; Zhong et al, 2015). We find this definition to be too restrictive for Mercury. The more open shape of the cusp and lower plasma density can weaken the diamagnetic depression in the cusp to render it unidentifiable in the field alone, while it is clearly visible in the plasma observations.

In Figures 2 and 3, we show four MESSENGER cusp crossings through time series of data from both FIPS and MAG. These are intended to illustrate the way that the cusp looks in this data, our identification and features in the precipitation flux. Figures 2 shows two typical cusp crossings by MESSENGER. In Fig. 2a, proton flux is enhanced through the cusp and reasonably well-separated from other features. The proton flux varies by over an order of magnitude through the different FIPS scans that make up the crossing, as is most evident as vertical blue-green stripes in the pitch angle distribution, where the measured plasma is largely isotropic. The proton precipitation flux varies over two orders of magnitude, largely following the overall measured proton flux though it is several orders of magnitude smaller. Diamagnetic depressions in the magnetic field are evident especially in the magnitude as short duration decreases (black arrows). The cusp is crossed at mid-latitudes and at altitudes around 320 km. Figure 2b shows cusp crossing where the energy spectrum displays a general energy dispersion
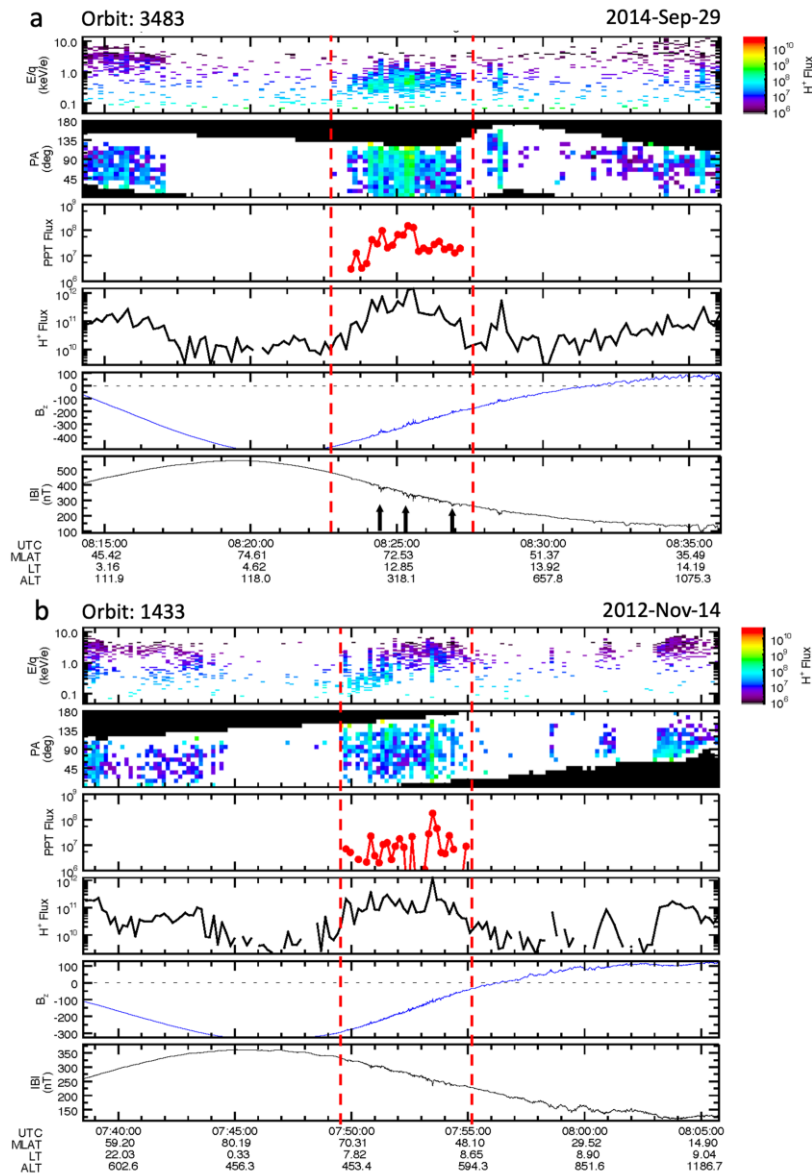
Figure 2. Observations during typical crossings of the northern magnetospheric cusp versus time (in UTC). In each subfigure, the top panel is an energy spectrogram, showing measured proton flux (in color, units of $(cm^2\ s\ sr\ keV/e)^{-1}$) at each E/q step through the cusp crossing. The second panel from the top is a pitch angle distribution for protons, in phase space density $(s^3\ m^{-6})$. The black region is the unobserved portion of pitch angle space for each timestep. The third panel from the top is the estimated precipitation flux $((cm^2\ s)^{-1})$. The fourth panel is measured proton flux $((cm^2\ s)^{-1})$ integrated over energy and angle. The remaining two panels show the Bz component of the magnetic field as well as the field magnitude (nT). Listed below the bottom panel are time (in UTC) and spacecraft position in magnetic latitude (degrees), local time (hours) and altitude (km). The dotted red lines correspond to the start (left) and stop (right) times of the cusp crossing. Black arrows identify diamagnetic decreases in the field strength.

feature: a decrease in low energies fluxes as magnetic latitude decrease (left to right), a feature

often observed in the cusp. Another notable feature of this crossing is that it displays highly variable flux in subsequent 10 s FIPS scans, visible as interspersed higher-flux streaks. Figure 3 displays two much more atypical examples. The crossing in Figure 3a shows a rare example of smoothly varying proton precipitation flux which follows the total proton flux early in the crossing but then continues to increase as more plasma is detected at low pitch angles (black bracket). The pitch angle distributions shown are similar to the ERPA (in Figure 1) but they are not separated by energy. Figure 3b shows a cusp crossing while the spacecraft was rotating, as evident in the sloping black boundaries that define FIPS FOV in pitch angle. Changes in the
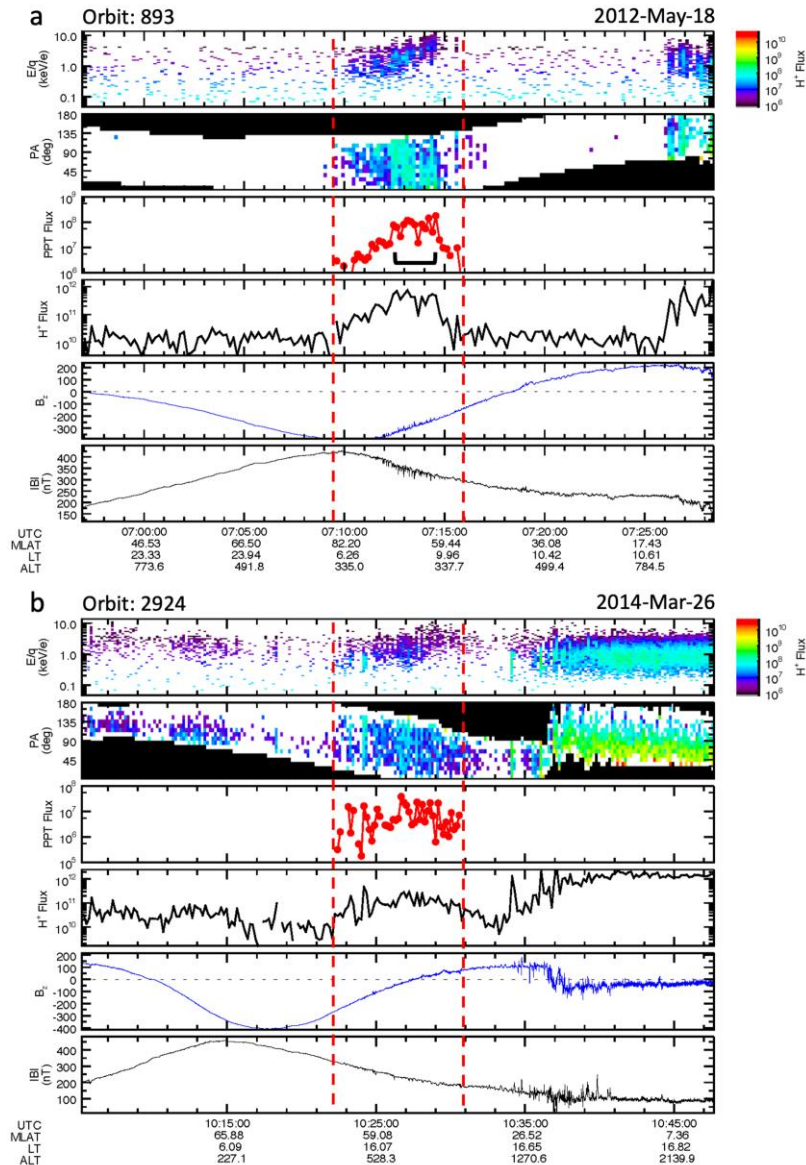

Figure 3.   Observations during two more unusual crossings of the northern magnetospheric cusp. The panels are identical to those in Figure 2. The black bracket shows a period of increased precipitation flux.

black portion of the plot show changes of FIPS orientation relative to the magnetic field. Since the magnetic field direction in the cusp is quite stable, these changes are mostly governed by changes in spacecraft orientation. This crossing also is notable for its low magnetic latitude, down to 38.4°. This crossing also illustrates one of the limitations of our boundary selection method (Appendix A): the right boundary does not occur at clear break in the proton flux, though it is coincident with end of the energy dispersion. Of course, these four crossings represent just a small fraction of the variable nature of Mercury's cusps.

     One of the most notable features of the estimated precipitation flux in this that it often varies significantly on the timescale of the FIPS 10 s energy scans, by as much as two orders of magnitude. This is evident in the red curves in the crossings shown in Figure 2. For this reason, it is clear that the average precipitation flux in this crossing does not tell the whole
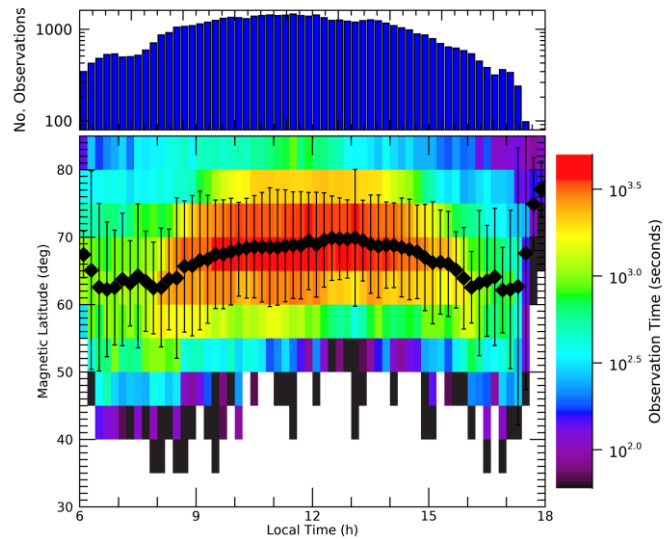

Figure 4. Observation time (seconds) in the cusp versus magnetic latitude (degrees) and local time for the 2760 cusps identified. The black diamonds mark the mean magnetic latitude for each local time column, and the black vertical lines denote the full width at half maximum of the histogram distribution in that column. The cusp generally extends to lower latitudes at local times more than 3 hrs from noon. The top panel shows the number of FIPS scans in each local time bin. The values for the last three bins (34, 24 and 6) are omitted for clarity.

story. We also have tabulated the peak precipitation flux, the maximum value for a particular crossing. For example, in Figure 2a the average, including scans with zero flux, is 3.4 x 10^7 (cm^2 s)$^{-1}$. The peak flux is 1.5 x 10^8 (cm^2 s)$^{-1}$, a factor of 4 larger. We further illustrate the mean and peak values in figures below and return to the variability of precipitation flux within a cusp crossing, at 10 s time scales, in the discussion.

6 Full Mission Analysis

6.1 Cusp Location and Extent

     We have identified the northern magnetospheric cusp in 2760 of the 4106 orbits with FIPS science data throughout the MESSENGER mission. This is all orbits possible using the criteria described in Section 5 and Appendix A. The remaining orbits were too closely aligned with the day-night terminator plane so that the cusp was either not crossed or not distinguishable from the thin slice observed. Of these 2760 cusps, 707 occurred when α = 0 was within the

FOV. The times for these crossings, as well as other information (described below), are listed in supporting information Table S1.

The average location and extent of the cusp is shown in Figure 4. In this figure, the area spanning 30-85° magnetic latitude and 6-18 hrs local time was divided into bins of 5° latitude and 0.2 hrs local time. For each cusp crossing, the count in each magnetic latitude bin crossed by the spacecraft was incremented for the (single) median local time of the crossing. The mean magnetic latitude for crossings in each local time column is marked with a black diamond, as well as a black vertical line showing the full width at half maximum of the histogram distribution in that column.

The resulting histogram shows some interesting features. The first is that the cusp is not likely circular. Crossing a circular cusp centered in this latitude range would lead to increasingly smaller areas crossed as the orbit plane neared the terminators, since the orbit plane precesses approximately around the geographic north pole. The cusp instead appears to be elliptical, with a long axis oriented roughly perpendicular to the noon-midnight meridian, so that a longer path is traversed farther from this plane. The ends of the oval cusp appear to be turned down as the mean magnetic latitude of the cusp drops from about 70° north near local noon to less than 65° north at local times more than 3 hrs from noon. This drop in mean magnetic latitude does not appear to be a projection effect. Forming a similar histogram versus altitude (not shown) yields in a largely uniform distribution of cusp altitude with local time, indicating that the behavior shown in Figure 4 is not due to changing altitude of cusp observations.

Histograms of cusp extent in magnetic latitude were constructed versus solar wind speed, IMF magnitude and IMF Bz (Figure 5). A top panel was added to each showing the number of observations in each column, since it was not at all uniform. Solar wind periods were selected by visually inspecting the proton energy distributions and magnetic field measurements well outside the bow shock. Periods where the proton distributions were narrow in energy (cold) that corresponded with steady magnetic field were identified as solar wind. A solar wind speed for the most representative 10-minute period, closest in time to the cusp crossing was estimated for each orbit using the method of Gershman et al. [2012]. The IMF vector was averaged over this period to produce the IMF magnitude and IMF Bz values. Correlations of measurements inside the magnetosphere, such as the cusp, with solar wind parameters must be evaluated in the
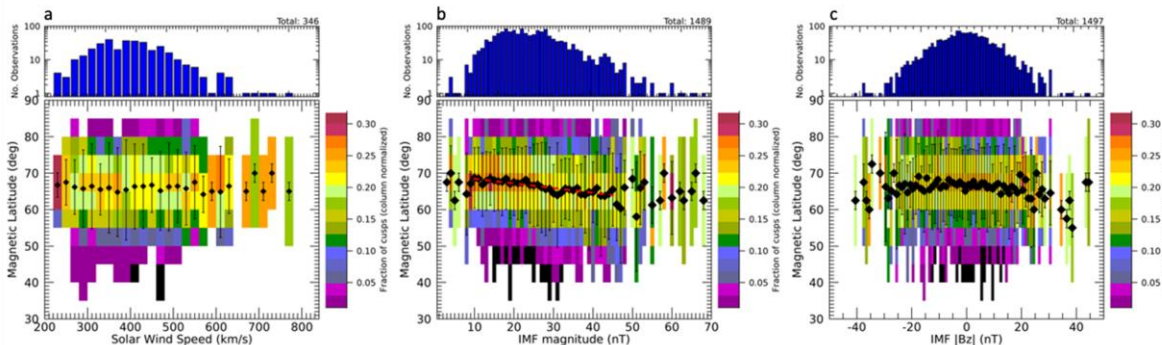

Figure 5. Cusp extent in magnetic latitude versus a) solar wind speed, b) IMF strength and c) IMF Bz. Histograms are constructed using the same procedure as for Figure 4. Black diamonds and vertical lines mark the column mean and full width at half maximum, respectively. Binning from left to right is 20 km/s, 1 nT and 1nT. Red dashed line in (b) shows linear fit to drop in cusp mean magnetic latitude with increasing magnetic field strength.

context that the latter can change in the intervening time between the measurements, typically about 100 min. in our analysis. Over a 2 hr interval, James et al. [2017] showed that the IMF magnitude had a 25% probability of changing by 20-35%. We find these values low enough to make correlations with solar wind speed and IMF magnitude still valuable. IMF variance would weaken the observed trends compared to those that might be observed with two simultaneous measurements, so these trends should be considered lower bounds. In contrast, the clock angle (angle in the Y-Z plane) had a 15-20% probability of changing by up to 60 degrees and a 5-15% probability of changing by up to 120 degree in a 20 min interval. This higher variability might explain the absence of any real trend in Fig. 5c.

There is subtle but systematic shift of the cusp center to lower latitudes as IMF magnitude increased to about 45 nT. A linear fit of this shift in the 10-45 nT range shows a drop of 1.3 degrees magnetic latitude for each increase of 10 nT in the IMF strength (red line in Figure 5b; intercept = 70°). Increased IMF magnitude results in a reduced upstream Alfvénic Mach number and consequently, lower plasma beta in the magnetosheath. These conditions enable large-scale plasma depletion and magnetic flux pile-up at the dayside magnetopause, resulting in increased reconnection rates. This may represent increased reconnection at the dayside magnetopause stripping away more and more of the dayside closed field region. This is consistent with the general result at Mercury that reconnection rate depends strongly on plasma depletion at the magnetopause [Slavin et al., 2009; Gershman et al., 2013; Jasinski et al, 2017]. Sun et al. [2020] added nuance to this finding with huge statistics, performing a detailed analysis of reconnection through flux transfer events (FTEs) in 3,748 dayside magnetopause crossings. They found that the rate and spacing of FTEs depends on both magnetic shear angle, the angle between the IMF and the planetary magnetic fields, and plasma beta, the ratio of plasma to magnetic pressure. A detailed comparison between that work and cusp properties, e.g. latitude, would be quite interesting and is left for future work.

This trend disappears at strengths >40 nT. This may be due to substantially lower statistics for these values of IMF strength (and those <10 nT). A downward slope may be apparent with IMF Bz value but it is not as well defined so no fit was performed. Neither cusp center nor extent in magnetic latitude show any systematic dependence on solar wind speed or the other components of the IMF.

6.2 Precipitation Flux

We applied the Section 4 method to proton flux measurements from each cusp for when $\alpha = 0$ was within the FOV, yielding a wide range of mean precipitating (PPT) fluxes, $3.3 \times 10^4 - 6.2 \times 10^8$ cm^{-2} s^{-1}, with a mean of 1.0×10^7 cm^{-2} s^{-1} (supporting information Table S1). These fluxes are plotted as a histogram in Figure 6. Since the fluxes are variable on the scale of a 10 s FIPS energy scan (demonstrated above), we show both the peak (red) and the mean precipitation flux (blue) for each individual cusp crossing. The peak value (red) is the flux from the scan with the highest precipitating flux for a single cusp crossing. Peak precipitation fluxes range $9.8 \times 10^4 - 1.4 \times 10^9$ cm^{-2} s^{-1}, with a mean of 3.7×10^7 cm^{-2} s^{-1}. Both the mean and peak values are highly variable, each spanning more than three orders of magnitude. Furthermore, the two distributions appear very similar, with the peak flux shifted to about 4 times higher than the mean.

We examined precipitation flux variability by comparing it to all spatial variables, both with regard to location of the cusp crossing and with Mercury's position in its orbit around the Sun (season). Since MESSENGER's orbit was fixed in inertial space, these two sets of variables are not independent. For instance, the cusp crossings around 12 hrs local time occurred when Mercury was about halfway between perihelion and aphelion, both on the orbital segments inbound to and outbound from the Sun. MESSENGER periapsis latitude was actively controlled by periodic propulsive maneuvers, so it is not as simply linked to season or other orbit parameters. The altitude of cusp crossing was a combination of the two: It was coupled to season like local time, with crossings at higher altitudes when Mercury was outbound from the Sun and MESSENGER had a nightside periapsis, but also affected by periodic propulsive maneuvers, which became more frequent during the last 9 months of the mission.
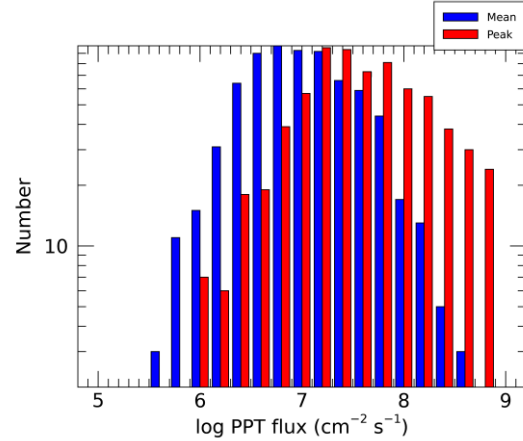

Figure 6. Histogram of proton precipitation flux observed throughout entire MESSENGER mission. Occurrence frequency for both mean (blue) and peak (red) fluxes are shown. This data represents 707 orbits of 2760 cusps when α=0 was in view.

Figure 7 shows the local time-seasonal dependence of precipitation flux. Although MESSENGER's local time-seasonal coverage was not complete (i.e., whitespace in Figure 7a), we note clear flux enhancements at smaller heliocentric distances (D) for fixed local times. For example, the cusps within the boxed regions sample the same local times but two sets of heliocentric distances centered on 0.353 ± 0.001 AU and 0.440 ± 0.002 AU. The typical mean precipitation fluxes of these cusps are $(6.2 \pm 0.7) \times 10^7$ cm^{-2} s^{-1} and $(3.0 \pm 0.2) \times 10^7$ cm^{-2} s^{-1}, respectively. The precipitation is not only greater when Mercury is closer to the Sun, but the increase exceeds that of the solar wind density. The flux increased by a factor of 2.1 ± 0.3. If the heliocentric trend in solar wind density (D^{-2}) dominates the change in precipitation, the flux should have increased by only 1.55 ± 0.03. We find similar behavior at all cusp local times. Figure 7b displays the ratio of precipitation flux for cusps below the horizontal dashed line in Figure 7a (Mercury's average heliocentric distance) to those above the line within each local time column. At all local times that have enough cusps for the comparison (>5), the increase in flux is within uncertainty of or exceeds that of the solar wind density (pink curve). Numerical fitting of these ratios results in a heliocentric trend of $D^{-3.6 \pm 0.6}$, indicating that additional processes to changes in solar wind density enhance cusp precipitation flux as Mercury approaches the Sun. We apply this heliocentric trend to complete the local time-seasonal coverage in Figure 7c. These extrapolated fluxes indicate that precipitation peaks near a local time of 11.5 hrs and that local time-seasonal trends account for 61% of variance in cusp precipitation. Seasonal trends contribute twice as much as local time trends to this variance. Finally, we applied the extrapolated flux to each cusp to remove local time and seasonal trends in precipitation. Using these detrended precipitation fluxes, we examined the distributions of precipitation versus cusp mean altitude as well as versus cusp magnetic latitude. We found no

trend in precipitation against either variable. On a related note, Jasinski et al. [2021] found that the seasonal variation of Na^+-group ions in the cusp is strongly tied to exospheric seasonal variation.
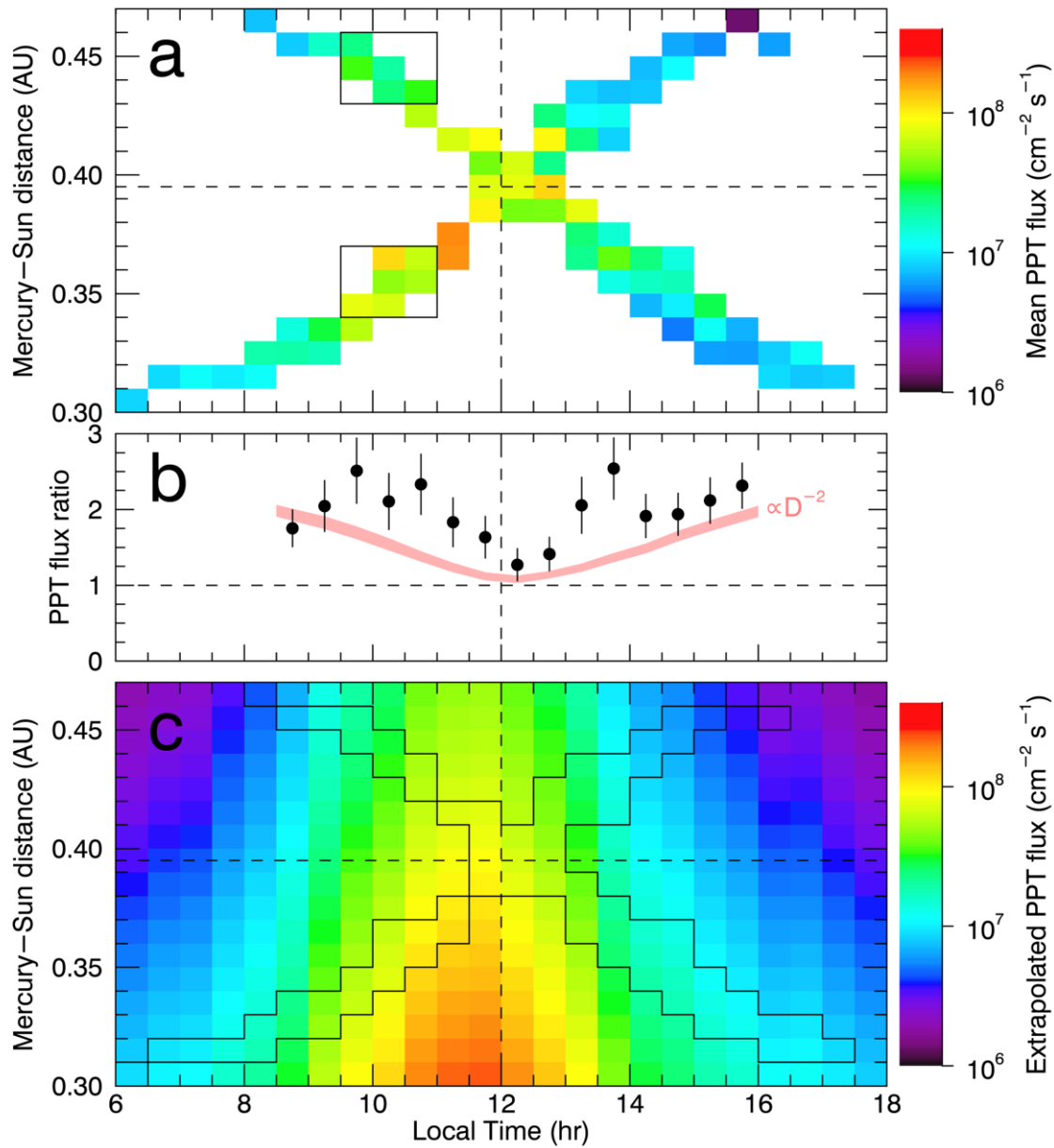
Figure 7. Proton precipitating flux variability with spatial and seasonal variables. (a) Precipitating flux versus cusp local time and heliocentric distance (D). (b) Flux ratio of cusps with $D < 0.395$ AU to those with $D > 0.395$ AU at each local time. Vertical lines represent variance in each measurement and the pink curve corresponds to a trend of D^{-2}. (c) Extrapolated local time-seasonal flux from measurements in (a) and fitted heliocentric dependence from (b). Bins with measurements in (a) are outlined. In all cases, only cusps with $\alpha = 0$ in view were included.

In Mercury's highly solar wind driven magnetosphere, the expectation is that the precipitation flux is mostly strongly controlled by the dayside magnetopause reconnection rate. As discussed above, determining these values for each of the 2760 cusps identified, or even the

707 for when α = 0 was within the FOV, is outside the scope of the current study. Instead, we compare precipitation flux with several possible proxies for dayside reconnection rate, IMF magnitude, IMF components (B_x, B_y, B_z), and solar wind velocity (determined for this study) as well as and a magnetospheric activity index [Anderson et al., 2013]. This index is an equally weighted composite of vector magnetic field variability from standard deviations over three periods, 0.1-2s, 2-20 s and 20-300 s, each representing groups of physical processes of interest. Solar wind speeds were determined for a single, 10 min, representative period for each orbit using the method of Gershman et al. [2012]. Averages of the IMF magnitude and components were computed for each of these periods.
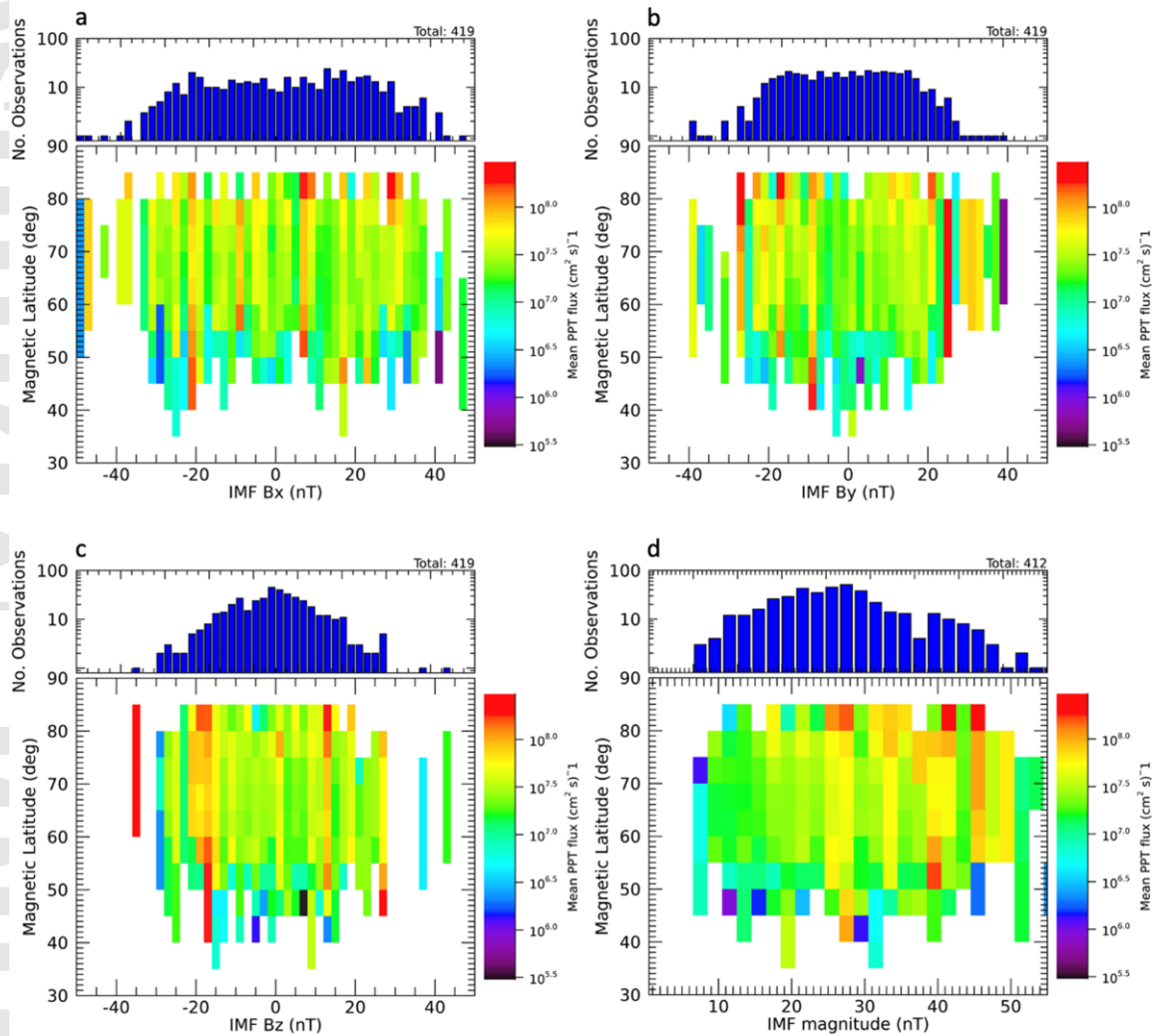

Figure 8. Dependence of precipitating proton flux on IMF strength and direction. The scale in panel d has been set to best show the bulk of the data; Seven points above 55 nT have been cutoff as a result.

We found that the strongest correlation with precipitation flux was with IMF strength and the By and Bz components. Precipitation flux increases fairly regularly with increasing IMF

magnitude up to 30 nT (Figure 7d), less so at higher IMF strengths. This result has been observed before, in a related context. Jasinski et al. [2017] found that the cross-tail potential increased with IMF magnitude. This potential is an indicator of reconnection rate on the dayside magnetopause, the same process that very likely controls plasma precipitation rate in the cusps, at least in part. Precipitation flux also increases with increasing |By| and |Bz|, somewhat more so for more negative values than more positive ones (Figure 7b and 7c). DiBraccio et al. [2013] showed that dayside reconnection is much less sensitive to magnetic shear angle at the dayside magnetopause at Mercury than at Earth. The latter has been said to respond as a "half-wave rectifier" [Burton et al., 1975; Slavin et al., 2014] because of the tight correlation between low-latitude magnetopause reconnection and southward (negative) IMF Bz. However, studies of extreme events at Mercury [Slavin et al. 2014; 2018] have indicated that prolonged southward IMF (e.g. IMF Bz<0) does lead to more reconnection and likely erosion of the dayside magnetosphere. The fact that Figure 7c shows higher precipitation fluxes for Bz<0 is consistent with those results. We found no clear dependence of proton precipitation rate on Bx (Figure 7a), solar wind speed (not shown) or magnetic activity index [Anderson et al., 2013] (not shown). He et al. [2017] developed another magnetic activity index. While also based on magnetic field fluctuations, this index includes only shorter period fluctuations (< 0.5 Hz) and includes a measure of anisotropy between fluctuations parallel and perpendicular to the magnetic field vector. These changes may make it a better indicator of the presence of proton instabilities, which may affect precipitation flux, though this interesting comparison is left for future work.

Because modeling often relies on knowledge of the precipitation rate, rather than just the flux, we estimated this quantity from the average precipitation flux on each cusp crossing. We assumed an average elliptical cusp centered at 12 h local time and 70º N in magnetic latitude, of a fixed size with a semi-major axis of 4 h and a semi-minor axis of 10º magnetic latitude (see Figure 4), at the mean altitude of all identified cusp crossings. This yields an average cusp area of 1.5E6 km^2. To remove local time effects in the observed precipitation rate resulting from MESSENGER's orbit, the average precipitation flux from each cusp crossing was scaled using the modeled local time-seasonal dependence from Figure 7c. Each crossing's average precipitation flux was divided by its modeled value in Figure 7c then multiplied by the 11.5-12 h local time value for that crossing's heliocentric distance. We further assumed that the average precipitation rate through the actual
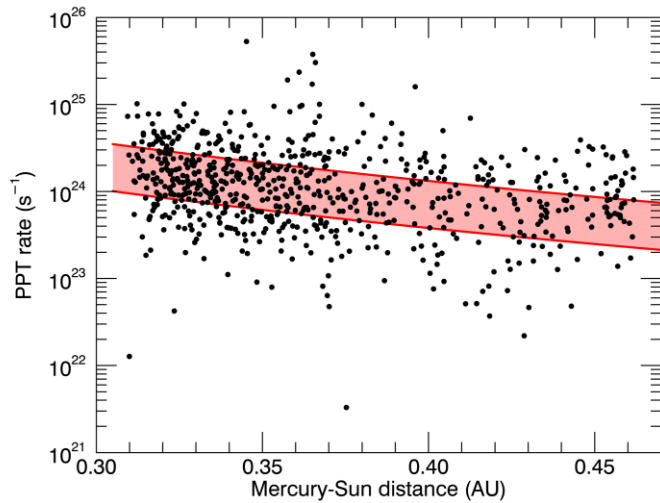

Figure 9. Estimated precipitation rate (s^{-1}) versus heliocentric distance (AU) using an average elliptical cusp area. Each black dot represents a different cusp crossing. The shaded red region indicates the range of typical values.

cusp crossing was representative of the entire cusp. This enabled us to estimate the precipitation rate by multiplying the assumed elliptical area by the scaled average flux, to arrive at the number of protons precipitating through a given cusp crossing per second. These values were plotted against Mercury's heliocentric distance in Figure 9. To represent the typical variability, we display modeled precipitation rates as the red shaded region in Figure 9. The lower bound uses the average flux over all local times from Figure 7c; the upper bound uses the maximum.

6.2.1 Time dependence

One interesting property of these cusp precipitation fluxes is that they are highly variable on the 10 s time scale of FIPS energy scans. The time series of precipitation fluxes
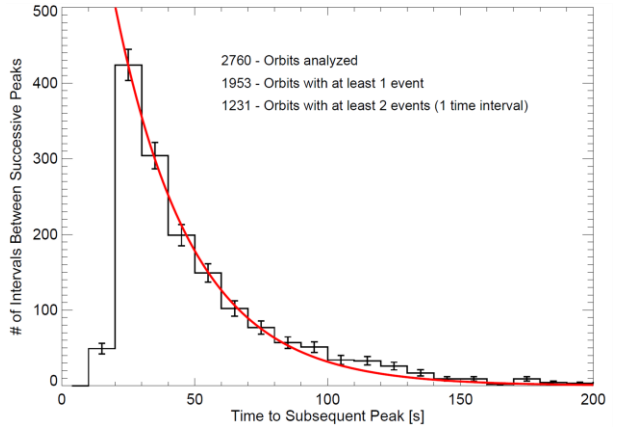

Figure 10. Histogram of peak separation intervals as identified using a 14% threshold, with $\pm\sqrt{N}$ error bars. Fitting the curve (red) of a Poisson random process to the data, we find on average that a peak appears once every 30 seconds.

in Figure 2 show this effect as large scan-by-scan (point-to-point) variations. To try to understand this variability, we analyzed the spacing between precipitation peaks, defined as scans where the precipitation flux exceeded a set percentage of the total flux measured within that cusp crossing. We found that choosing a threshold of 14% of the total precipitation flux (in that cusp crossing) reliably discriminated peaks from background. For cusp crossings with at least two peaks, we computed the difference in time between all successive peaks present in that cusp crossing. We refer to these as peak separation intervals. We accumulated such intervals for all cusp crossings into a histogram, choosing 10 s bins to match the natural 10-11 s spacing of FIPS energy scans and computed a histogram of peak separations (Figure 10). We found 1521 peak separation intervals distributed across 1231 orbits.

We find the distribution of intervals is well described as by a Poisson random process, where the rate at which peaks occur is found to be approximately once every 30 seconds. A Poisson random process is any random process characterized by a constant probability of occurrence per unit time. The distribution of durations between peaks following a Poisson random process is described by

$$N(t) = (Cn)\, e^{-rt}\, r$$

where $N(t)$ is the number of occurrences, r is the occurrence rate, t is the duration between peaks, n is the total histogram population in Figure 10, and C is a coefficient such that the product Cn expresses total population including missing observations of intervals less than 20 seconds long. Limitations to this analysis stem from systematic error in the measurement of observation time and the minimum resolution (10-11 seconds) of a full FIPS scan. When identifying peaks, if multiple adjacent FIPS scans exceed the threshold, we considered there to have been a single, extended peak and take an average of the scans' start times. For these reasons, the algorithm never identifies intervals shorter than 10 seconds and we have chosen to exclude the 10-20 second intervals from the fit.

Weighting the fit by inverse square root of bin population (total histogram population n=1522), we find values C = 1.9073 ± 0.0008 [scalar] and r = 2.072 ± 0.002 [arrivals per minute]. These results show that the spacing between precipitation peaks is well-described as random, with a mean arrival time of about 30 s and about half of peak separations occurring more rapidly than FIPS completed scans. The variations likely arise from changes in reconnection rate and the number of reconnection sites on the dayside magnetopause due variations in solar wind pressure and IMF strength and direction. Analyses of reconnection rates on Mercury's dayside indicate that the time scale of individual reconnection events is much shorter than the observed inter-peak spacing, at most seconds [Slavin et al., 2008; 2010; DiBraccio et al., 2013]. FTE showers [Slavin et al., 2010] and plasma filaments [Poh et al., 2016] represent this in the extreme and are not resolvable using the methods of this work.

7   Discussion

There are two main differences between this work and the past predictions from modeling. First, the estimated average flux here is 1-2 orders of magnitude lower than model predictions, though those predictions are within the range of values reported here. Second, our measurements indicate precipitating fluxes are highly variable spatiotemporally, both within a single cusp crossing and between multiple crossings. This extreme variability has not yet been captured in the models and may well be the reason for the higher fluxes models predict. Some models, e.g. Fatemi el al. [2020, Figure 2d], Kallio and Janhunnen [2003, Figure 3a-c], and Masetti et al. [2003, Figure 5] do capture the broad extent of the cusp in local time especially, as observed in Figure 4. The global average precipitation flux was estimated previously from FIPS observations [Winslow et al., 2014]. That study used FIPS pitch angle distributions to estimate an average precipitation rate and surface magnetic field for each cusp. Based on early estimates of the average cusp proton density and temperature [Zurbuchen et al., 2011; Raines et al., 2014], Winslow et al. estimated a mean precipitation flux in the northern hemisphere at 3.7×10^8 cm^{-2} s^{-1}. This is much higher than reported here, but understandably so. The variability that we now see could not have been captured using their methods, which were designed primarily to determine the mean magnetic field strength at the surface.

As discussed above, the precipitating fluxes in this work are estimates: These protons were not observed actually impacting the surface, though all spacecraft-based *in situ* observations are subject to this same limitation. The most significant assumption required for this estimate is that the ions behave adiabatically. Deviations from adiabatic behavior in the cusp would affect the accuracy of our predictions. Delcourt et al. [1994] showed that under certain conditions, protons can depart from adiabatic behavior in the cusp. These deviations generally resulted in scattering of particles *into* the loss cone, and thus increasing precipitation flux. When this behavior happens at altitudes above the MESSENGER observations in the cusp, they would still be captured in our estimates. When it happens below the observation altitude, the estimates from FIPS measurements would tend to be underestimates. More work would be required to evaluate the true impact of these effects on the estimates presented in this work.

7.1   Uncertainties

In order to make these estimates as accurate as possible, most of this study has been focused on cusp crossings where the magnetic field direction is within the FOV, at least for much of the crossing. This should ensure that we are making the best estimates possible from the data. It is

still true that a hot distribution could be cutoff by the limited FOV. This would result in an error factor of order of the cutoff portion of hemispherical solid angle (2π sr). Since FIPS unobstructed FOV is ~1.15π sr, this factor should be $< 0.8\pi$ sr. Given that the proton precipitation flux often changes by more than a factor of 10 on successive 10 s FIPS energy scans, we are confident that the error due to possibly cutoff distributions does not change our conclusions nor does it substantially reduce the usefulness of our estimates for other studies. Statistical errors are much smaller, estimated at less than 30% for over 90% of the cusp crossings. The rest are marked with a low statistics flag in Table S1.

7.2   Implications for the southern hemisphere

Our study focused on proton precipitation fluxes in the northern hemisphere because MESSENGER's orbit passed closely by this region throughout the mission. Our results do not pertain directly to precipitation at the southern cusp. However, an order of magnitude comparison between the two cusps is probably best accomplished via the work of Winslow et al. [2014]. In the southern cusp, their analysis of the proton loss cone indicated that the surface field was significantly weaker than in the northern cusp, by a factor of 2-10 including uncertainties. That fact should lead to a greater proton precipitation flux in the southern hemisphere, though it is beyond the scope of this work to estimate those values from our scan by scan observations. It is important to note that they report a smaller precipitation flux, 4.4×10^7 cm^{-2} s^{-1}, in the southern cusp as compared to 3.7×10^8 cm^{-2} s^{-1} in the northern cusp.   The fact that the flux in the southern cusp is lower is counter intuitive based on the weaker field. However, this is likely a result of the much higher altitude of the observations used for this estimate, which leads to much larger uncertainties in the proton density, loss cone size and diffusion factor.

We can also use model results as a guide to extrapolating these results to the southern hemisphere. Fatemi et al. [2020] showed that precipitation flux through the southern cusp is 2-10x higher than through the northern cusp. The IMF Bz and Bx components were found to be largely the controlling factors, with the highest ratios occurring when Bx was pointed in the sunward (positive) direction.

8   Summary and Conclusions

In this work, we have identified the northern magnetospheric cusp in 2760 of MESSENGER's 4106 orbits of Mercury, using enhancements in proton flux measured by FIPS. This represents the full set of crossings that can be identified with our method. We found that the mean latitude of the northern cusp dropped as IMF magnitude increased, from 68° at 10 nT to 63° at 45 nT. We computed estimates of the precipitating proton flux for all of these orbits, assuming adiabatic behavior and adjusting for the altitude of the spacecraft where the plasma measurements were taken. We found an average proton precipitation flux of 1.0×10^7 cm^{-2} s^{-1} and that this flux typically varies between subsequent measurements. To represent this variation, we tabulated peak values, the largest precipitation flux value in a single 10 s scan, as well as mean values for each orbit analyzed. We found that precipitation flux was not significantly organized by cusp altitude or magnetic latitude. It does show a strong dependence on heliocentric distance and local time. Using representative values for each orbit, we also compared proton precipitation flux with solar wind speed and IMF parameters. We found that precipitation flux generally increased with increasing IMF $|B_y|$, $|B_z|$ and $|B|$, while no clear trend

with IMF |B$_x$| was evident. Finally, we analyzed the spacing between precipitation peaks on time scale of FIPS 10 s energy scans. We found that this spacing fit well to a Poisson distribution indicating that it is well described as a random process.

9 Open Research

All data used in this study are available at NASA's Planetary Data System, MAG v6 and EPPS FIPS v1. The data can be found at the following URL: https://pds-ppi.igpp.ucla.edu/search/?sc=Messenger&i=EPPS-FIPS.

10 Acknowledgements

11 Appendix A: Cusp boundary refinement algorithm

We developed a software algorithm to regularize and trim cusp boundaries identified first by eye. By-eye boundaries were selected following the criteria of Raines et al. (2014) using time series plots that spanned the magnetosphere crossing (~1-2 hours duration). At this zoom, recording times were accurate to ±1-2 minutes. Therefore, we applied a software algorithm to improve the accuracy of the cusp times, remove natural inconsistency from by-eye approaches, and root the boundaries in precise FIPS scan times. The algorithm refined each cusp boundary by assessing the similarity of FIPS scans with the cusp and finding the concentration of these scans compared to the surrounding magnetospheric measurements. An example of the algorithm applied to a cusp crossing is shown in Figure A1.

First, each cusp was divided in time into five regions based on the cusp's by-eye start time (t_1), stop time (t_2), and duration (Δt). These regions correspond to the shaded intervals in the middle panel.

(1) $[t_1 + 0.2\Delta t, t_2 - 0.2\Delta t]$, central cusp (purple)
(2) $[t_1 - 0.2\Delta t, t_1 + 0.2\Delta t]$, early boundary (red)
(3) $[t_2 - 0.2\Delta t, t_2 + 0.2\Delta t]$, late boundary (green)
(4) $[t_1 - 1.2\Delta t, t_1 - 0.2\Delta t]$, pre-cusp (cyan)
(5) $[t_2 + 0.2\Delta t, t_2 + 1.2\Delta t]$, post-cusp (yellow)

We cut regions (4) and (5) short if they cross into the magnetosheath or nightside magnetosphere (grey regions).

Next, plasma characteristics were used to determine cusp-like FIPS scans in each region. Given the variability and diversity in cusp signatures, particularly in plasma flux and energy distribution (see Figure 2), we used the number of E/q steps with ≥ 2 proton counts ($N_{E/q}$) to determine the similarity of each FIPS scan. For (1), FIPS scans were assigned "cusp-like" if

$N_{E/q} \geq 2$. The low threshold for (1) was used since this region represents the central and most reliably identified interval. For (2), cusp-like scans require $N_{E/q}$ greater than the mean $N_{E/q}$ of region (4). Likewise, cusp-like scans in (3) require $N_{E/q}$ greater than the mean $N_{E/q}$ of region (5). These criteria were established to identify FIPS scans in (2) and (3) that contain a broader plasma distribution than the surrounding non-cusp regions.

Finally, the software used the time series of cusp-like scans to refine the boundaries. For the earlier (later) cusp boundary, the algorithm started at the earliest (latest) cusp-like scan in (1). From the starting scan, the refined boundary would be the earliest (latest) cusp-like scan such that there were no more than three non-cusp-like scans between the starting scan and the refined boundary. This approach allowed for spatiotemporal variability within the cusp and allowed for the edges of the cusp, which usually contain less plasma than the center, to be more accurately captured. In the example in Figure A1, the algorithm expanded the earlier boundary to capture two additional scans while it trimmed the later boundary by nearly a minute as a result of the comparison between those scans and the plasma in the closed dayside region (yellow).

Refining the cusp boundaries via algorithm standardized cusp boundaries (including the trimming of empty scans near the cusp) and rooted the boundaries to a precise FIPS scan time. We found that the algorithm performed well and returned accurate boundaries to within ±10-20 seconds (±1-2 scans) except in a small number of cases (0.9%), typically when penetrating radiation would inflate $N_{E/q}$ and result in too generous of boundaries. The refined boundaries are listed in supporting information Table S1. We encourage readers to examine the boundaries before use and modify them based on the aim of their particular study.
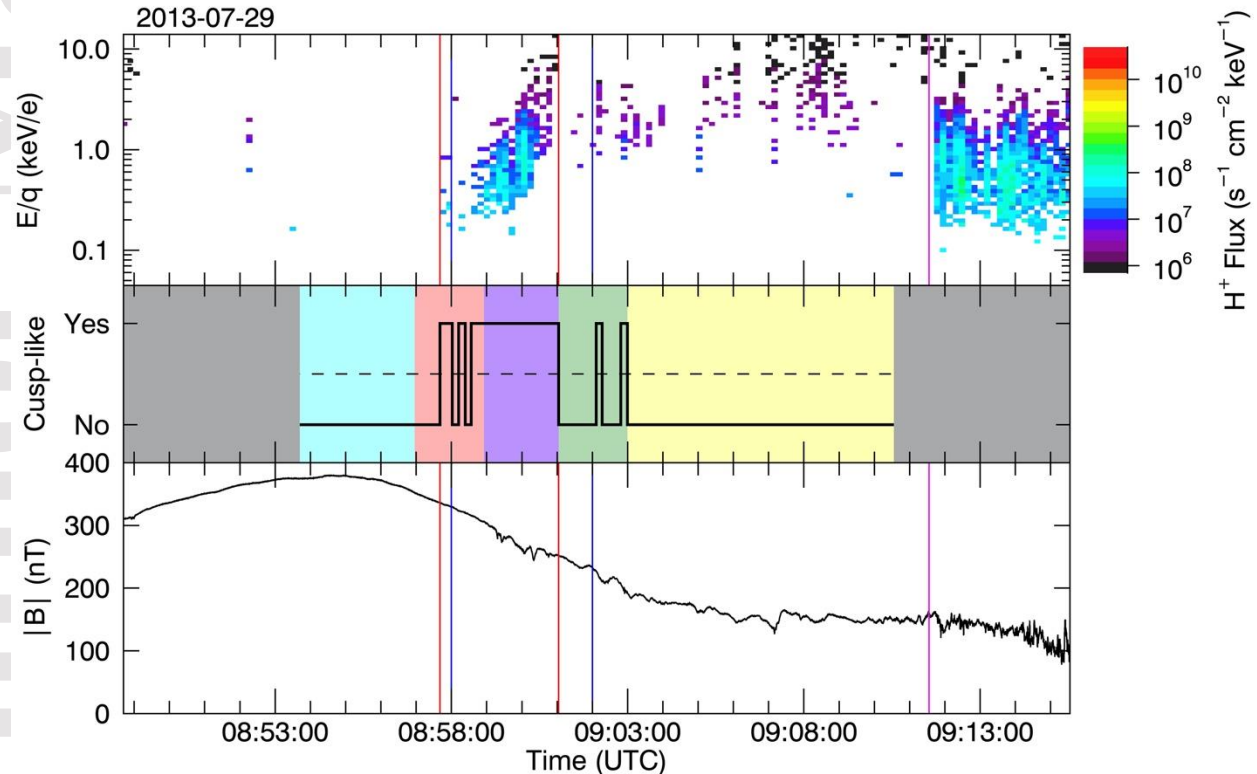

Figure A1. An example of cusp boundaries identified by eye (vertical blue lines) and refined by the software algorithm (vertical red lines). (top) Proton flux spectrogram, (middle) algorithm

regions and cusp-like scans (see text), and (bottom) magnetic field strength. The vertical magenta line marks the magnetopause.

7. References

Acton, C.H. (1996), "Ancillary Data Services of NASA's Navigation and Ancillary Information Facility;" *Planet Space Sci.*, Vol. 44, No. 1, pp. 65-70.

Acton, C. H., N. Bachman, B. Semenov, E. Wright (2017), A look toward the future in the handling of space science mission geometry, *Planet Space Sci.*, Vol. 150, January 2018, pp. 9-12, doi:10.1016/j.pss.2017.02.013.

Anderson, B. J., M. H. Acuna, D. A. Lohr, J. Scheifele, A. Raval, H. Korth, and J. A. Slavin (2007), The Magnetometer instrument on MESSENGER, *Space Sci. Rev., 131*, 417-450.

Anderson, B. J., et al. (2011), The global magnetic field of Mercury from MESSENGER orbital observations, *Science, 333,* 1859–1862, doi:10.1126/science.1211001.

Anderson, B. J., C. L. Johnson, and H. Korth (2013), A magnetic disturbance index for Mercury's magnetic field derived from MESSENGER Magnetometer data, Geochemistry, Geophysics, Geosystems, 14, 3875-3886, doi: 10.1002/ggge.20242.

Andrews, G. B., et al. (2007), The Energetic Particle and Plasma Spectrometer instrument on the MESSENGER spacecraft, *Space Sci. Rev., 131*, 523–556, doi:10.1007/s11214-007-9272-5.

Benna, M., et al., (2010), Modeling of the magnetosphere of Mercury at the time of the first MESSENGER flyby, *Icarus, 209*, 3–10, doi:10.1016/j.icarus.2009.11.036.

Burger, M. H., R. M. Killen, W. E. McClintock, R. J. Vervack Jr., A. W. Merkel, A. L. Sprague, and M. Sarantos (2012), Modeling MESSENGER observations of calcium in Mercury's exosphere, J. Geophys. Res.*, 117*, E00L11, doi:10.1029/2012JE004158.

Burger, M. H., R. M. Killen, W. E. McClintock, A. W. Merkel, R. J. Vervack, Jr., T. A. Cassidy, and M. Sarantos (2014), Seasonal variations in Mercury's dayside calcium exosphere, *Icarus, 238*, 51–58.

Burton, R. K., R. L. McPherron, and C. T. Russell (1975), The Terrestrial Magnetosphere: A Half-Wave Rectifier of the Interplanetary Electric Field, Science, 189, 717-718, doi: 10.1126/science.189.4204.717.

Cassidy, T. A., A. W. Merkel, M. H. Burger, M. Sarantos, R. M. Killen, W. E. McClintock, and R. J. Vervack (2015), Mercury's seasonal sodium exosphere: MESSENGER orbital observations, Icarus, 248, 547-559, doi: 10.1016/j.icarus.2014.10.037.

Delcourt, D. C., R. F. Martin, and F. Alem (1994), A simple model of magnetic moment scattering in a field reversal, Geophysical Research Letters, 21, 1543-1546, doi: 10.1029/94GL01291.

Dewey, R. M., J. M. Raines, W. Sun, J. A. Slavin, and G. Poh (2018), MESSENGER Observations of Fast Plasma Flows in Mercury's Magnetotail, Geophysical Research Letters, 45, 10,110-10,118, doi: 10.1029/2018GL079056.

DiBraccio, G. A., J. A. Slavin, S. A Boardsen, B. J. Anderson, H. Korth, T. H. Zurbuchen, J. M. Raines, D. N. Baker, R. L. McNutt Jr., and S. C. Solomon (2013), MESSENGER observations of magnetopause structure and dynamics at Mercury, *J. Geophys. Res. Space Physics, 118*, 997–1008, doi:10.1002/jgra.50123.

Domingue, D. L., P. L. Koehn, R. M. Killen, A. L. Sprague, M. Sarantos, A. F. Cheng, E. T. Bradley, and W. E. McClintock (2007), Mercury's atmosphere: A surface-bounded exosphere, *Space Sci. Rev., 131*, 161–186.

Domingue, D. L., C. R. Chapman, R. M. Killen, T. H. Zurbuchen, J. A. Gilbert, M. Sarantos, M. Benna, J. A. Slavin, D. Schriver, P. M. Trávníček, T. M. Orlando, A. L. Sprague, D. T. Blewett, J. J. Gillis-Davis, W. C. Feldman, D. J. Lawrence, G. C. Ho, D. S. Ebel, L. R. Nittler, F. Vilas, C. M. Pieters, S. C. Solomon, C. L. Johnson, R. M. Winslow, J. Helbert, P. N. Peplowski, S. Z. Weider, N. Mouawad, N. R. Izenberg, and W. E. McClintock (2014), Mercury's Weather-Beaten Surface: Understanding Mercury in the Context of Lunar and Asteroidal Space Weathering Studies, Space Science Reviews, 181, 121-214, doi: 10.1007/s11214-014-0039-5.

Fatemi, S., N. Poirier, M. Holmström, J. Lindkvist, M. Wieser, and S. Barabash (2018), A modelling approach to infer the solar wind dynamic pressure from magnetic field observations inside Mercury's magnetosphere, Astronomy and Astrophysics, 614, A132, doi: 10.1051/0004-6361/201832764.

Fatemi, S., A. R. Poppe, and S. Barabash (2020), Hybrid Simulations of Solar Wind Proton Precipitation to the Surface of Mercury, Journal of Geophysical Research (Space Physics), 125, e27706, doi: 10.1029/2019JA027706.

Gloeckler, G., J. Cain, F. M. Ipavich, E. O. Tums, P. Bedini, L. A. Fisk, T. H. Zurbuchen, P. Bochsler, J. Fischer, R. F. Wimmer-Schweingruber, J. Geiss, and R. Kallenbach (1998), Investigation of the composition of solar and interstellar matter using solar wind and pickup ion measurements with SWICS and SWIMS on the ACE spacecraft, Space Science Reviews, 86, 497-539, doi: 10.1023/A:1005036131689.

Gershman, D. J., T. H. Zurbuchen, L. A. Fisk, J. A. Gilbert, J. M. Raines, B. J. Anderson, C. W. Smith, H. Korth, and S. C. Solomon (2012), Solar wind alpha particles and heavy ions in the inner heliosphere observed with MESSENGER, Journal of Geophysical Research (Space Physics), 117, A00M02, doi: 10.1029/2012JA017829.

Gershman, D. J., J. A. Slavin, J. M. Raines, T. H. Zurbuchen, B. J. Anderson, H. Korth, D. N. Baker, and S. C. Solomon (2013), Magnetic flux pileup and plasma depletion in Mercury's subsolar magnetosheath, Journal of Geophysical Research (Space Physics), 118, 7181-7199, doi: 10.1002/2013JA019244.

Gershman, D. J., J. A. Slavin, J. M. Raines, T. H. Zurbuchen, B. J. Anderson, H. Korth, D. N. Baker, and S. C. Solomon (2014), Ion kinetic properties in Mercury's pre-midnight plasma sheet, Geophysical Research Letters, 41, 5740-5747, doi: 10.1002/2014GL060468.

Gershman, D. J., J. M. Raines, J. A. Slavin, T. H. Zurbuchen, B. J. Anderson, H. Korth, G. C. Ho, S. A. Boardsen, T. A. Cassidy, B. M. Walsh, and S. C. Solomon (2015), MESSENGER observations of solar energetic electrons within Mercury's magnetosphere, Journal of Geophysical Research (Space Physics), 120, 8559-8571, doi: 10.1002/2015JA021610.

Gershman, D. J., J. C. Dorelli, G. A. DiBraccio, J. M. Raines, J. A. Slavin, G. Poh, and T. H. Zurbuchen (2016), Ion-scale structure in Mercury's magnetopause reconnection diffusion region, Geophysical Research Letters, 43, 5935-5942, doi: 10.1002/2016GL069163.

Gershman, D. J., A. F-Viñas, J. C. Dorelli, S. A. Boardsen, L. A. Avanov, P. M. Bellan, S. J. Schwartz, B. Lavraud, V. N. Coffey, M. O. Chandler, Y. Saito, W. R. Paterson, S. A. Fuselier, R. E. Ergun, R. J. Strangeway, C. T. Russell, B. L. Giles, C. J. Pollock, R. B. Torbert, and J. L. Burch (2017), Wave-particle energy exchange directly observed in a kinetic Alfvén-branch wave, Nature Communications, 8, 14719, doi: 10.1038/ncomms14719.

He, M., J. Vogt, D. Heyner, and J. Zhong (2017), Solar wind controls on Mercury's magnetospheric cusp, Journal of Geophysical Research (Space Physics), 122, 6150-6164, doi: 10.1002/2016JA023687.

Imber, S. M., J. A. Slavin, S. A. Boardsen, B. J. Anderson, H. Korth, R. L. McNutt Jr. and S. C. Solomon (2014), MESSENGER observations of large dayside flux transfer events: Do they drive Mercury's substorm cycle?, *J. Geophys. Res Space Physics, 119*, 5613–5623, doi:10.1002/2014JA019884.

James, M. K., S. M. Imber, E. J. Bunce, T. K. Yeoman, M. Lockwood, M. J. Owens, and J. A. Slavin (2017), Interplanetary magnetic field properties and variability near Mercury's orbit, Journal of Geophysical Research (Space Physics), 122, 7907-7924, doi: 10.1002/2017JA024435.

Jasinski, J. M., Slavin, J. A., Raines, J. M., & DiBraccio, G. A. (2017). Mercury's solar wind interaction as characterized by magnetospheric plasma mantle observations with MESSENGER. Journal of Geophysical Research: Space Physics, 122, 12153– 12169. https://doi.org/10.1002/2017JA024594

Jasinski, J. M., Cassidy, T. A., Raines, J. M., Milillo, A., Regoli, L. H., Dewey, R., et al. (2021). Photoionization loss of Mercury's sodium exosphere: Seasonal observations by MESSENGER and the THEMIS telescope. Geophysical Research Letters, 48, e2021GL092980. https://doi.org/10.1029/2021GL092980

Kallio, E., and P. Janhunen (2003), Modelling the solar wind interaction with Mercury by a quasi-neutral hybrid model, *Ann. Geophys., 21*, 2133.

Killen, R., G. Cremonese, H. Lammer, S. Orsini, A. E. Potter, A. L. Sprague, P. Wurz, M. Khodachenko, H. I. M. Lichtenegger, A. Milillo, and A. Mura (2007), Processes that Promote and Deplete the Exosphere of Mercury, *Space Sci. Rev. 132*, 433–509.

Killen, R. M., A. E. Potter, R. J. Vervack, E. T. Bradley, W. E. McClintock, C. M. Anderson, and M. H. Burger (2010), Observations of metallic species in Mercury's exosphere, Icarus, 209, 75-87, doi: 10.1016/j.icarus.2010.02.018.

Lammer, H., P. Wurz, M. R. Patel, R. M. Killen, C. Kolb, S. Massetti, S. Orsini, and A. Milillo (2003), The variability of Mercury's exosphere by particle and radiation induced surface release processes, *Icarus, 166*, 238–247.

Lavraud, B., A. Fedorov, E. Budnik, A. Grigoriev, P. Cargill, M. Dunlop, H. Rème, I. Dandouras, and A. Balogh (2004), Cluster survey of the high-altitude cusp properties: a three-year statistical study, Annales Geophysicae, 22, 3009-3019, doi: 10.5194/angeo-22-3009-2004.

Lavraud, B., H. Rème, M. W. Dunlop, J.-M. Bosqued, I. Dandouras, J.-A. Sauvaud, A. Keiling, T. D. Phan, R. Lundin, P. J. Cargill, C. P. Escoubet, C. W. Carlson, J. P. McFadden, G. K. Parks, E. Moebius, L. M. Kistler, E. Amata, M.-B. Bavassano-Cattaneo, A. Korth, B. Klecker, and A. Balogh (2005), Cluster Observes the High-Altitude CUSP Region, Surveys in Geophysics, 26, 135-175, doi: 10.1007/s10712-005-1875-3.

Leblanc, F., and R. E. Johnson (2003), Mercury's sodium exosphere, *Icarus, 164*, 261–281, doi:10.1016/S0019-1035(03)00147-7.

Madey, T. E., B. V. Yakshinskiy, V. N. Ageev, and R. E. Johnson (1998), Desorption of alkali atoms and ions from oxide surfaces: Relevance to origins of Na and K in atmospheres of Mercury and the Moon, Journal of Geophysical Research, 103, 5873-5888, doi: 10.1029/98JE00230.

Mangano, V., S. Massetti, A. Milillo, C. Plainaki, S. Orsini, R. Rispoli, and F. Leblanc (2015), THEMIS Na exosphere observations of Mercury and their correlation with in-situ magnetic field measurements by MESSENGER, Planetary and Space Science, 115, 102-109, doi: 10.1016/j.pss.2015.04.001.

Massetti, S., S. Orsini, A. Milillo, A. Mura, E. De Angelis, H. Lammer, and P. Wurz (2003), Mapping of the cusp plasma precipitation on the surface of Mercury, *Icarus, 166*, 229–237.

McLain, J. L., A. L. Sprague, G. A. Grieves, D. Schriver, P. Travnicek, and T. M. Orlando (2011), Electron-stimulated desorption of silicates: A potential source for ions in Mercury's space environment, *J. Geophys. Res., 116*, E03007, doi:10.1029/2010JE003714.

Merkel, A. W., T. A. Cassidy, R. J. Vervack, W. E. McClintock, M. Sarantos, M. H. Burger, and R. M. Killen (2017), Seasonal variations of Mercury's magnesium dayside exosphere from MESSENGER observations, Icarus, 281, 46-54, doi: 10.1016/j.icarus.2016.08.032.

Milillo, A., P. Wurz, S. Orsini, D. Delcourt, E. Kallio, R. M. Killen, H. Lammer, S. Massetti, A. Mura, S. Barabash, G. Cremonese, I. A. Daglis, E. Angelis, A. M. Lellis, S. Livi, V. Mangano, and K. Torkar (2005), Surface-Exosphere-Magnetosphere System Of Mercury, Space Science Reviews, 117, 397-443, doi: 10.1007/s11214-005-3593-z.

Orsini, S., V. Mangano, A. Milillo, C. Plainaki, A. Mura, J. M. Raines, E. De Angelis, R. Rispoli, F. Lazzarotto, and A. Aronica (2018), Mercury sodium exospheric emission as a proxy for solar perturbations transit, Scientific Reports, 8, 928, doi: 10.1038/s41598-018-19163-x.

Pfleger, M., H. I. M. Lichtenegger, P. Wurz, H. Lammer, E. Kallio, M. Alho, A. Mura, S. McKenna-Lawlor, and J. A. Martín-Fernández (2015), 3D-modeling of Mercury's solar wind sputtered surface-exosphere environment, Planetary and Space Science, 115, 90-101, doi: 10.1016/j.pss.2015.04.016.

Poh, G., J. A. Slavin, X. Jia, G. A. DiBraccio, J. M. Raines, S. M. Imber, D. J. Gershman, W.-J. Sun, B. J. Anderson, H. Korth, T. H. Zurbuchen, R. L. McNutt, and S. C. Solomon (2016), MESSENGER observations of cusp plasma filaments at Mercury, Journal of Geophysical Research (Space Physics), 121, 8260-8285, doi: 10.1002/2016JA022552.

Potter, A. E., R. M. Killen, and M. Sarantos (2006), Spatial distribution of sodium on Mercury, *Icarus, 181*, 1–12.

Raines, J. M., D. J. Gershman, J. A. Slavin, T. H. Zurbuchen, H. Korth, B. J. Anderson, and S. C. Solomon (2014), Structure and dynamics of Mercury's magnetospheric cusp: MESSENGER measurements of protons and planetary ions, *J. Geophys. Res. Space Physics, 119*, 6587–6602, doi:10.1002/2014JA020120.

Sarantos, M., R. M. Killen, and D. Kim (2007), Predicting the long-term solar wind ion-sputtering source at Mercury, Planetary and Space Science, 55, 1584-1595, doi: 10.1016/j.pss.2006.10.011.

Sarantos, M., R. M. Killen, W. E. McClintock, E. T. Bradley, R. J. Vervack, M. Benna, and J. A. Slavin (2011), Limits to Mercury's magnesium exosphere from MESSENGER second flyby observations, *Planet. Space Sci., 59*, 1992–2003.

Slavin, J. A., et al. (2008), Mercury's magnetosphere after MESSENGER's first flyby, *Science, 321*, 85–89, doi:10.1126/science.1159040.

Slavin, J. A., et al. (2009), MESSENGER observations of magnetic reconnection in Mercury's magnetosphere*, Science, 324,* 606–610.

Slavin, J. A., et al. (2010), MESSENGER observations of extreme loading and unloading of Mercury's magnetic tail*, Science, 329,* 665–668.

Slavin, J. A., G. A. DiBraccio, D. J. Gershman, S. M. Imber, G. K. Poh, T. H. Zurbuchen, X. Jia, D. N. Baker, S. A. Boardsen, M. Sarantos, T. Sundberg, A. Masters, C. L. Johnson, R. M. Winslow, B. J. Anderson, H. Korth, R. L. McNutt Jr., and S. C. Solomon (2014), MESSENGER observations of Mercury's magnetosphere under extreme solar wind conditions, *J. Geophy. Res. Space Physics, 119*, 8087–8116, doi:10.1002/2014JA020319.

Solomon, S. C., R. L., McNutt, R. E. Gold, and D. L. Domingue (2007), MESSENGER: Mission Overview, *Space Sci. Rev., 131*, 3–39.

Sonnerup, B. U. O., G. Paschmann, I. Papamastorakis, N. Sckopke, G. Haerendel, S. J. Bame, J. R. Asbridge, J. T. Gosling, and C. T. Russell (1981), Evidence for magnetic field reconnection at the earth's magnetopause, Journal of Geophysical Research, 86, 10049-10067, doi: 10.1029/JA086iA12p10049.

racy, P. J. (2016), In-situ plasma analysis of ion kinetics in the solar wind and hermean magnetosphere, Ph.D. Thesis, doi:.

Vervack, R. J., W. E. McClintock, R. M. Killen, A. L. Sprague, B. J. Anderson, M. H. Burger, E. T. Bradley, N. Mouawad, S. C. Solomon, and N. R. Izenberg (2010), Mercury's complex exosphere: Results from MESSENGER's third flyby, *Science, 329*, 672–675, doi:10.1126/science.1188572.Vervack 2016

Wiens, R. C., D. S. Burnett, W. F. Calaway, C. S. Hansen, K. R. Lykke, and M. J. Pellin (1997), Sputtering Products of Sodium Sulfate: Implications for Io's Surface and for Sodium-Bearing Molecules in the Io Torus, Icarus, 128, 386-397, doi: 10.1006/icar.1997.5758.

Winslow, R. M., C. L. Johnson, B. J. Anderson, H. Korth, J. A. Slavin, M. E. Purucker, and S. C. Solomon (2012), Observations of Mercury's northern cusp region with MESSENGER's Magnetometer, *Geophys. Res. Lett., 39*, L08112, doi:10.1029/2012GL051472.

Winslow, R. M., et al. (2014), Mercury's surface magnetic field determined from proton-reflection magnetometry, *Geophys. Res. Lett., 41*, 4463–4470, doi:10.1002/2014GL060258.

Yashinskiy and Madey, 2000, Thermal desorption of sodium atoms from thin SiO2 films, *Surf. Rev. Lett., 7*, 75–87.

Zhong, J., W. X. Wan, J. A. Slavin, Y. Wei, R. L. Lin, L. H. Chai, J. M. Raines, Z. J. Rong, and X. H. Han (2015), Mercury's three-dimensional asymmetric magnetopause, Journal of Geophysical Research (Space Physics), 120, 7658-7671, doi: 10.1002/2015JA021425.

Zurbuchen, T. H., et al. (2011), MESSENGER observations of the spatial distribution of planetary ions near Mercury, *Science, 333*, 1862.

Tracy, P. J. (2016), In-situ Plasma Analysis of Ion Kinetics in the Solar Wind and Hermean Magnetosphere, Ph.D. Thesis.

ProQuest Dissertations And Theses; Thesis (Ph.D.)--University of Michigan, 2016.; Publication Number: AAT 10391814; ISBN: 9781369590234; Source: Dissertation Abstracts International, Volume: 78-07(E), Section: B.; 257 p.

Sun, W. J., J. A. Slavin, A. W. Smith, R. M. Dewey, G. K. Poh, X. Jia, J. M. Raines, S. Livi, Y. Saito, D. J. Gershman, G. A. DiBraccio, S. M. Imber, J. P. Guo, S. Y. Fu, Q. G. Zong, and J. T. Zhao (2020), Flux Transfer Event Showers at Mercury: Dependence on Plasma β and Magnetic Shear and Their Contribution to the Dungey Cycle, Geophysical Research Letters, 47, e89784, doi: 10.1029/2020GL089784.